

3D CFD simulations of wind flow and wind-driven rain shelter in sports stadia: influence of stadium geometry

T. van Hooff ^{(a,b),1*}, B. Blocken ^(a), M. van Harten ^(a)

(a) Building Physics and Systems, Eindhoven University of Technology, P.O. Box 513, 5600 MB Eindhoven, The Netherlands

(b) Laboratory of Building Physics, Katholieke Universiteit Leuven, Kasteelpark Arenberg 40, 3001 Leuven, Belgium

Abstract

Sports stadia are increasingly used to host a wide variety of activities that attract large attendances, ranging from sports matches to concerts, festivities and conferences. One of the crucial aspects of spectator comfort in open stadia is protection from wind and rain. However, in many stadia this part of spectator comfort is insufficiently taken care of. The main reason is that stadia and stadium roofs are often designed with only vertical rainfall in mind, neglecting the influence of wind that can sweep the rain onto the stands. This wind-driven rain (WDR) can reach a large area of the stand underneath the roof, resulting in discomfort for the spectators in this area. For stadium design, it is important to understand the interaction between wind and rain in different types of stadium geometry and its effect on wetting of the stands.

This paper presents 3D Computational Fluid Dynamics (CFD) simulations of wind flow and WDR for twelve different generic stadium configurations that are representative for a wide range of existing stadia. The wind-flow patterns are determined by steady-state Reynolds-averaged Navier-Stokes (RANS) simulations. The WDR trajectories are calculated using Lagrangian particle tracking, yielding the wetting pattern on the stands. This study demonstrates the influence of both overall stadium geometry and roof slope on the area of the stand that is wetted by WDR. It shows the importance of taking into account WDR in the stadium design process, and it provides some design guidelines to avoid this type of spectator discomfort.

Keywords: Wind-driven rain; Driving rain; Sports stadium; Computational Fluid Dynamics (CFD); Parameter study; Rain protection

1. Introduction

Since the first stadium was built in ancient Greece, sports stadia have always been impressive works of building engineering [1]. For contemporary stadium designs, spectator comfort is an important design parameter. One of the most important aspects of spectator comfort in open stadia (where only the stands are covered by a roof) is the protection from weather influences such as wind and rain. However, the majority of stadia are built with only vertical rainfall in mind, neglecting the influence of wind that can sweep the rain onto the stands. This wind-driven rain (WDR) can reach a large area of the stand underneath the roof, resulting in discomfort for the spectators in this area. The statement that stadia are usually only built with vertical rainfall in mind is supported by the fact that the roof generally does not reach further than the separation between the stands and the field. Ignoring the influence of the wind and WDR during stadium design can give rise to discomfort for the spectators that are seated in the lower regions of the stand, due to insufficient protection from WDR.

The construction of many new (semi-)open stadia has incited research on spectator comfort in these stadia. Szücs et al. [2] assessed the visual comfort of spectators in a generic stadium configuration by numerical simulations using a daylight program. This study focused on the influence of roof inclination angle on the daylight distribution on the pitch. Szücs et al. [3,4] studied the effect of wind flow on thermal comfort in generic stadium configurations by wind tunnel measurements. Among others, they analyzed the effect of facade porosity and roof inclination angle on the wind-flow pattern inside the stadium and concluded that the wind velocity in the stadium can be altered significantly by design changes to the stadium facades and roofs. Bouyer et al. [5] coupled the results of climatic, airflow and thermo-radiative modules in an Enriched Virtual Environment (EVE) to predict the thermal comfort level in the Atatürk stadium in Istanbul, Turkey and the Stade de France in Paris,

¹ Twan van Hooff is a PhD student at both Eindhoven University of Technology and the Katholieke Universiteit Leuven.

* Corresponding author: Twan van Hooff, Building Physics and Systems, Eindhoven University of Technology, P.O. box 513, 5600 MB Eindhoven, the Netherlands. Tel: +31 (0)40 247 5877, Fax: +31 (0)40 243 8595. *E-mail address:* t.a.j.v.hooff@tue.nl

France. These studies assumed a uniform air temperature and relative humidity distribution to assess the influence of solar irradiation and wind velocity on thermal comfort. Bouyer et al. [5] used either a uniform wind-velocity field inside the stadia or a wind-velocity field based on wind tunnel measurements for one of the prevailing wind directions. From their calculations, they concluded that higher wind speeds can have a positive effect on thermal comfort in stadia, especially when high radiant temperatures are present. To the knowledge of the authors, the first WDR study in stadia was published by Persoon et al. [6]. They performed 2D CFD simulations to assess the WDR shelter for seven generic stadium configurations. The study showed that the roof design can strongly influence the size of the wetting areas on the stands. However, as mentioned in that study, 3D CFD simulations should be performed in order to capture the real 3D flow pattern and to provide a better assessment of the influence of roof geometry on WDR shelter. Van Hooff and Blocken [7] conducted CFD simulations to study natural ventilation by wind and buoyancy in the large semi-enclosed Amsterdam Arena stadium in the Netherlands. Configurations with different ventilation openings were analyzed to increase the air change rate. In a later study, van Hooff and Blocken [8] assessed the influence of wind direction and urban surroundings on the natural ventilation of the same stadium, indicating the strong effect of these parameters on the air change rates.

The use of CFD to study the interaction between wind and rain has become increasingly common since the pioneering work by Choi in the nineties. To the knowledge of the authors, CFD has up to now been applied for three types of WDR studies: (1) WDR on building facades; (2) WDR on small-scale topographic features such as hills and valleys; and (3) WDR on the stands of football stadia.

By far, most CFD studies of WDR focused on WDR impingement on building facades. A review of these studies, up to 2003, has been provided by Blocken and Carmeliet [9]. Choi [10-13] developed and applied a steady-state simulation technique for WDR, in which the wind-flow field is modeled using the Reynolds-Averaged Navier-Stokes (RANS) equations with a turbulence model to provide closure. The raindrop trajectories are determined by solving the equation of motion of raindrops of different sizes in the wind-flow pattern. In 2002, Blocken and Carmeliet [14] extended Choi's steady-state simulation technique into the time domain, allowing WDR simulations for real-life transient rain events. Some first CFD validation studies of the steady-state technique were performed by Hangan [15] and van Mook [16]. The extension of Choi's technique into the time domain allowed detailed validation studies to be performed based on full-scale WDR measurements from real-life transient rain events. The first study of this type was made by Blocken and Carmeliet [14] for a low-rise test building. Later, the same authors performed more detailed validation studies for the same building [17,18]. In 2004, the extended WDR simulation method by Blocken and Carmeliet was also used by Tang and Davidson [19] to study the WDR distribution on the high-rise Cathedral of Learning in Pittsburgh. Later validation studies by Abuku et al. [20] for a low-rise building and Briggen et al. [21] for a tower building also used this method.

The steady-state CFD technique for WDR was also employed to study the distribution of WDR over small-scale topographic features such as hills and valleys [22-25]. Arazi et al. [22] compared CFD simulations of WDR in a small valley with the corresponding measurements. Choi [23] modeled WDR impingement on idealized hill slopes. Blocken et al. [24] simulated WDR distributions on sinusoidal hill and valley slopes. Finally, Blocken et al. [25] performed validation of CFD simulations of the WDR distribution over four different small-scale topographic features: a succession of two cliffs, a small hill, a small valley and a field with ridges and furrows.

To the knowledge of the authors, the only publication about CFD WDR simulation in football stadia is that by Persoon et al. [6], who used 2D CFD simulations to study the rain shelter by stadium roofs. However, 3D CFD studies are required for a detailed analysis of the wind-flow patterns and WDR patterns in stadia.

As indicated by the literature review above, studies on comfort in stadia so far did not include 3D WDR shelter. However, rain shelter is a crucial aspect of spectator comfort. The literature review also indicated that the vast majority of CFD WDR studies were performed to assess the WDR intensity on building facades and on the slopes of small-scale topographic features. To the knowledge of the authors, only one simplified 2D study was performed on WDR in stadia [6]. Especially for WDR in stadia, there is an important knowledge gap, and more information is needed. The specific shapes of stadia, with an open roof and sometimes also open corners, will give rise to particular wind-flow patterns and therefore also specific WDR distributions that are largely unknown and very difficult to predict without using CFD.

In this paper, 3D steady-state CFD simulations are presented of wind flow and WDR for twelve generic stadium configurations. All configurations are based on the same stand cross-section and overall stadium dimensions. The flow field is modeled using the RANS equations in combination with the realizable $k-\epsilon$ turbulence model [26] to provide closure. The choice for this turbulence model is based on previous validation studies and on existing recommendations for CFD simulations, as will be explained in section 3. The simulations are conducted for a reference wind speed U_{10} at 10 m height of 10 m/s and for wind perpendicular to the long edges of the stadium. Lagrangian particle tracking in the wind-flow pattern is used to obtain trajectories of raindrops of 0.5, 1, 2 and 5 mm diameter. The performance of the different stadium configurations is evaluated based on the percentages of wetted surface area on the stands. This study is intended to provide support for future stadium research and stadium design. Stadium research is expected to increase significantly due to the

increasing number of new multifunctional stadia that are planned and the increasing awareness that these very specific buildings should provide the highest level of comfort to the spectators. It is important to realize that wetting by rain is a very severe type of discomfort, which is generally not taken into account in comfort studies in general and comfort studies in stadia in particular.

The paper consists of 7 sections. Section 2 presents the twelve generic stadium configurations. Section 3 contains the results of previous CFD validation studies of WDR to support the application of CFD in the present paper. In Section 4, the computational model and simulation parameters are outlined. The simulation results are reported and discussed in Section 5. Finally, Section 6 (discussion) and Section 7 (summary and conclusions) conclude the paper.

2. Description of generic stadium configurations

The stadium configurations in this study are based on the stadium of football club AZ in Alkmaar, the Netherlands (Fig. 1a-b). The stadium has a capacity of about 17,000 spectators. Its exterior dimensions are 176.8 x 138 x 22.5 m³ (L x W x H) (Fig. 1a) and it has a downward sloped roof with an inclination of 13° (Fig. 1b). This type of roof was intuitively chosen by the architects to improve shelter from WDR. The stands consist of one tier that is present along the entire perimeter of the stadium, with a height of about 16 m.

The stand cross-section (without roof) in the present study is taken equal to that of the AZ stadium (Fig. 1c). The cross-section is equipped with one of three different roof types (upward sloped roof, flat roof and downward sloped roof) (Fig. 1d). The three roof types are combined with four different stand arrangements, yielding twelve different stadium configurations (Fig. 2). Note that the roof angle for both the upward and downward sloped roof is 13° (Fig. 1d), and that for all roof types, the roof extends just beyond the first row of the stand, so that the stand will not be wetted in case of vertical rainfall.

3. Previous CFD validation studies

The intention of this section is to indicate that a given combination of computational settings and parameters has led to fairly accurate CFD simulations of WDR in the past, and that therefore the same combination will be applied in the present paper. This combination consists of: (1) For wind-flow simulation: a computational domain that is large enough (see [27,28]), a computational grid based on grid-sensitivity analysis, steady RANS simulations with the realizable k- ϵ model [26], standard [29] or non-equilibrium [30] wall functions modified for roughness, second order discretization schemes and the SIMPLE algorithm for pressure-velocity coupling. (2) For WDR: the raindrop-size distribution by Best [31], the drag coefficients by Gunn and Kinzer [32] and piecewise analytical integration of the raindrop equation of motion with a maximum length-step $L = 0.05$ m [17]. While several validation studies have been performed in the past [14-22, 25], only the results of studies that used the above-mentioned combination are mentioned below.

A comparison of CFD simulations of WDR with full-scale measurements on the facade of a low-rise test building (Fig. 3a-b) indicated deviations in WDR amount of on average 20% [17,18]. The wind direction was perpendicular to the facade. Note that 20% is considered a good agreement given the complexity of both turbulent flow around a building and WDR deposition on building surfaces. A similar study, for another low-rise test building but for various wind directions, showed facade surface-averaged deviations of 17%, 25% and 31% for wind incidence angles of 5, 18 and 34°, respectively [20]. The wind incidence angle is the angle between the wind direction and the normal to the windward facade. The deviations clearly increase with increasing incidence angle. For both studies, a good qualitative agreement was found. Brüggen et al. [21] compared CFD WDR results on the south-west facade of a tower building with full-scale measurements. A good agreement was found at the upper part of the facade (20% on average), but very large discrepancies were found at the lower part of the south-west facade (up to more than a factor 2). This was attributed to the effect of turbulent dispersion, which can be especially important for the bottom part of high-rise buildings and when the reference wind speed is low. Blocken et al. [25] compared CFD simulations of WDR deposition over small-scale topographic features such as hills and valleys (Fig. 3c-h) with full-scale measurements. The deviations between simulation and measurement results were on average 15%, 4% and 10% for a hill, a valley and a succession of ridges, respectively. For each case, a good qualitative and quantitative agreement was obtained. Overall, CFD simulations on the facades of low-rise buildings and the upper part of a high-rise building and on three different small-scale topographic features have shown that the above-mentioned combination of computational parameters for wind and WDR can yield good qualitative and fairly accurate quantitative results. The same combination will be applied in the study in the present paper.

4. Computational model

4.1. Computational geometry and grid

The geometry of the stadium configurations is as discussed in Section 2. The computational domain has dimensions 1100 x 973 x 500 m³ (L x W x H) (Fig. 4), resulting in a blockage ratio of 0.7%, which is below the recommended maximum value of 3% by Franke et al. [27] and Tominaga et al. [28]. The distance from the stadium to the sides and top of the domain is at least five times the height of the stadium, and the distance from the outlet is at least fifteen times the height, according to the guidelines by Franke et al. [27] and Tominaga et al. [28]. The height and upstream distance of the domain are larger than the distance of 5H suggested by these guidelines: the height of the domain is 500 m and the upstream distance is 400 m to allow the injection of raindrops upstream and above the wind-flow pattern that is affected by the stadium.

For efficient generation of high-quality grids, the procedure presented by van Hooff and Blocken [7] is used. In this procedure, only one single master grid is created in which all stadium geometries and grids are embedded a priori. The master grid is generated by a series of surface extrusion operations, i.e. creating the geometry and the grid based on geometrical translation operations of pre-meshed 2D cross-sections. It results in a hybrid grid of hexahedral and prismatic cells, in which tetrahedral cells are avoided, which is beneficial for convergence behavior. Another important advantage of this procedure is the full control of grid quality and resolution. By deleting the designated meshed volumes from the master grid, each of the twelve different stadium configurations is obtained. Figure 5 shows the computational grid near the stands and roof. The grid resolution in the vicinity of the roof was increased for a more detailed prediction of the wind flow in this area compared to the remainder of the domain. The dotted lines in Figure 5 indicate which volume grids have to be deleted to obtain roof type 1, 2 and 3 respectively. The computational grid for the four stand arrangements combined with a flat roof is shown in Figure 6. More detailed information on the grid generation procedure can be found in van Hooff and Blocken [7]. The grids are based on grid-sensitivity analysis (see Section 4.3).

4.2. Boundary conditions, turbulence model and solver settings

At the inlet of the domain, a power-law mean wind speed profile representing a neutral atmospheric boundary layer (ABL) is imposed with a power-law exponent α of 0.15 and a reference wind speed $U_{10} = 10$ m/s (Eq. (1)).

$$\frac{U}{U_{10}} = \left(\frac{y}{y_{10}} \right)^{\alpha} \quad (1)$$

The power-law exponent α of 0.15 corresponds to an aerodynamic roughness length y_0 of about 0.03 m, which represents a uniformly rough, grass-covered terrain [33]. The turbulence intensity I_U ranges from 20% at 2 m height to 5% at gradient height. Turbulent kinetic energy k is calculated from I_u and U assuming $\sigma_v \ll \sigma_u$ and $\sigma_w \ll \sigma_u$:

$$k = 0.5 I_U U^2 \quad (2)$$

The turbulence dissipation rate ε is calculated by:

$$\varepsilon = \frac{u_{ABL}^{*3}}{\kappa y + y_0} \quad (3)$$

where y is the height coordinate, κ the von Karman constant ($\kappa = 0.42$) and u_{ABL}^* the friction velocity for the ABL flow.

The CFD code Fluent 6.3.26 [34] is used to solve the 3D steady RANS equations in combination with the realizable k - ε turbulence model [26] to provide closure. While it is known that modeling external flows is not straightforward with linear eddy-viscosity models, almost all earlier CFD WDR validation studies were performed with this category of models. More specifically, these studies used the realizable k - ε model [14,17,18,25] and the Renormalization Group (RNG) k - ε model [19]. The realizable k - ε model is selected for the study in this paper for three reasons:

1. It contains significant improvements compared to the standard k-ε model. The term “realizable” refers to mathematical constraints on the normal stresses that are satisfied by the model: positivity of normal stresses and Schwarz inequality for shear stresses. Like the RNG k-ε model, also the realizable model attenuates the stagnation point anomaly without leading to worse results in the wake, compared to the standard k-ε model [26,35].
2. The realizable k-ε model has been validated for a wide range of flows including separated flows and has been found to perform substantially better than the standard k-ε model [26,33]. The same conclusion was reached by a literature study with recommendations on the use of CFD in wind engineering. In these recommendations, Franke et al. [36] advise the use of more advanced linear eddy-viscosity models such as the realizable k-ε model.
3. Last but not least, the use of the realizable k-ε model has lead to a good agreement between CFD WDR simulations and full-scale measurements in different validation studies covering a substantial range of buildings and topographic features (Fig. 3), as explained in section 3.1. Note that, even when there are discrepancies in the wind-flow pattern, raindrop trajectories will be less sensitive to small discrepancies due to the inertia of the raindrops.

For near-wall treatment, the standard wall functions by Launder and Spalding [29] are used with the sand-grain based roughness modification by Cebeci and Bradshaw [37]. The parameters k_s and C_s are determined from their appropriate relationship with y_0 , derived by Blocken et al. [38] for Fluent and CFX. For Fluent 6, up to at least version 6.3, this relationship is given by:

$$k_s = \frac{9.793 y_0}{C_s} \quad (4)$$

The value of k_s is limited by Fluent to the height of the centre point of the wall-adjacent cell y_p , which is 0.5 m for this study. In order to limit horizontal inhomogeneity of the approach mean wind speed profile, C_s was set to 0.584 to satisfy Eq. (4). Note that the y^* value, $y^* = (y_p u^*)/\nu$, with ν the kinematic viscosity and u^* the friction velocity, is about 15,000-20,000, which significantly exceeds the recommended value of 500-1,000. However, standard wall functions are typically also used in CFD simulations of atmospheric boundary layer wind flow when y^* is well above the upper limit of 500-1,000 without reduced performance for the velocity field (see for example [38] for simulations with $y^* = 15,609$). This is also demonstrated in previous validated CFD studies in which y^* values with the same order of magnitude were used [7,8]. The most important reason for using these high y^* values is that the recommended range of y^* values (30-500) would yield unnecessarily small near-wall cells. The stadium surfaces are set to have zero roughness height ($k_s = 0$). This is a simplification of reality, since the stands are stair-shaped and often equipped with seats. However, the influence of the roughness of the stand will mainly have an effect on the local air flow near the seats, while the main wind-flow pattern in and around the stadium, as well as the raindrop trajectories will hardly be altered by this modeling simplification. Earlier research [7,8] on wind flow in stadia has indeed shown that a good agreement between velocity measurements and CFD simulations can be obtained with the $k_s = 0$ assumption. In this earlier research, parametric CFD studies with k_s values of 0, 0.01 m and 0.05 m also showed no notable differences for the wind-flow pattern. The top of the computational domain is modeled as a slip wall (zero normal velocity and zero normal gradients of all variables) and zero static pressure is imposed at the outlet. The SIMPLE algorithm is used for pressure-velocity coupling, pressure interpolation is standard and second order discretization schemes are used for both the convection terms and the viscous terms of the governing equations.

After the steady wind-flow field has been obtained, the raindrop trajectories are calculated using Lagrangian particle tracking, which implies solving the equation of motion of a raindrop that is moving in a wind-flow field. The forces acting on a raindrop are the gravitational force, the drag force and the Archimedes force (Fig. 7). Newton’s second law yields:

$$\vec{F}_g + \vec{F}_D + \vec{F}_A = m \frac{d^2 \vec{r}}{dt^2} \quad (5)$$

with m the mass of the raindrop, \vec{r} the position vector of the raindrop in xyz-space and t the time coordinate. F_g is the gravitational force on the raindrop:

$$\vec{F}_g = m\vec{g} = \rho_w \frac{\pi d^3}{6} \vec{g} \quad (6)$$

with g the gravitational acceleration, ρ_w the density of the raindrop and d the raindrop diameter. The drag force is :

$$\vec{F}_D = \frac{1}{2} \rho_a C_d A \left(\vec{U} - \frac{d\vec{r}}{dt} \right) \left\| \vec{U} - \frac{d\vec{r}}{dt} \right\| \quad (7)$$

with ρ_a the density of air, C_d the raindrop drag coefficient, A the surface area of the raindrop and \vec{U} the mean velocity vector. The Archimedes force is:

$$\vec{F}_A = -\rho_a V \vec{g} = -\rho_a \frac{\pi d^3}{6} \vec{g} \quad (8)$$

with V the volume of the raindrop. Inserting Eqs. 6-8 in Eq. 5 yields the equation of motion of the raindrop:

$$\left(\frac{\rho_w - \rho}{\rho_w} \right) \vec{g} + \frac{3\mu}{\rho_w d^2} \frac{C_d Re_R}{4} \left(\vec{U} - \frac{d\vec{r}}{dt} \right) = \frac{d^2 \vec{r}}{dt^2} \quad (9)$$

where Re_R is the relative Reynolds number (referring to the airflow around the drop):

$$Re_R = \frac{\rho d}{\mu} \left\| \vec{U} - \frac{d\vec{r}}{dt} \right\| \quad (10)$$

with μ the dynamic viscosity of air. Four raindrop diameters are considered in this study: $d = 0.5$ mm, 1 mm, 2 mm and 5 mm, which are raindrops taken from raindrop spectra that represent rainfall varying from drizzle to a heavy shower [31].

4.3. Grid-sensitivity analysis

The grid-sensitivity analysis, as part of CFD solution verification, is performed for the configuration with two stands and a flat roof by using three different grids with 553,568 cells (coarse grid), 1,490,489 cells (middle grid) and 3,734,178 cells (fine grid), respectively. Comparison of the results from the three grids is performed based on the dimensionless velocity magnitude U/U_{10} on three lines ($\alpha\alpha'$), ($\beta\beta'$) and ($\gamma\gamma'$) inside the stadium (Fig. 8a). U/U_{10} is the ratio of the magnitude of the 3D wind velocity vector to the reference wind speed U_{10} at 10 m height. The lines ($\alpha\alpha'$) and ($\beta\beta'$) are located in the region of the stadium that is traversed by the raindrops that impinge on the downstream stand. Figures 8b-d illustrate U/U_{10} for the three lines. The results obtained with the middle grid are almost equal to the results of the fine grid. The results of the coarse grid however show a larger deviation from the results of the middle grid, for all three lines (Fig. 8b-d). Therefore the middle grid was chosen as the basis for the simulations for the twelve stadium configurations.

5. Results

5.1. Wind-flow patterns

5.1.1. Wind-flow patterns in a horizontal plane

Figure 9 and 10 show the wind-flow patterns in a horizontal plane at a height of 1 m above ground level for four stadium configurations, all equipped with a flat roof (configurations A2, B2, C2, D2; see Fig. 2). Figure 9 displays the wind-velocity vectors, while Figure 10 shows the contours of the dimensionless velocity magnitude U/U_{10} . Note that the velocity vectors in the different figures do not have the same scale. The following observations are made:

- Configuration A2 (Fig. 9a): Two large counter-rotating vortices are situated between the upstream and downstream stand. They are mainly driven by the corner stream shear layer originating at the corners of the upstream stand.
- Configuration B2 (Fig. 9b): The flow pattern is very similar to that for configuration A2. The stands that are present on the short edges of the stadium influence the flow inside the stadium only to a small extent. The reason is that the side flow is not totally obstructed by these stands and can pass through the area between the stand and the roof. Nevertheless, higher velocities are present in the upstream corners of the stadium than for A2 (Fig. 10a-b).

- Configuration C2 (Fig. 9c): The addition of windshields on the sides of all stands results in a flow pattern that is significantly different. The horizontal counter-rotating vortices on the field are no longer present. The windshields block the flow that comes around the corner of the upstream stand and jets with high velocities are formed (Fig. 10c), which are directed to the center of the stadium. The jet flow is the result of the combination of two corner streams (one from each corner).
- Configuration D2 (Fig. 9d): Two main vortices are present inside the stadium, but compared to the first two configurations, these vortices are smaller and have lower velocities (Fig. 10d). The flow pattern inside the stadium is more complex than the other three configurations due to the presence of additional small vortical structures above the field and underneath the roof, which are partly visible in Figure 9d, and partly in Figure 11d.

The flow patterns in the horizontal plane at 1 m height, as described above, are also found for the stadium configurations with a downward and upward sloped roof.

5.1.2. Wind-flow patterns in the vertical center plane

Figure 11 shows the wind-flow pattern in a vertical cross-section through the middle of the upstream and downstream stand ($z = 60$ m).

- Configuration A2 (Fig. 11a): The presence of the two large near-ground vortices results in a flow from the downstream stand to the upstream stand. A vortex is also present in the vertical plane between the roof edges. This vortex does not reach the ground plane and its center is located above roof height.
- Configuration B2 (Fig. 11b): Almost identical to configuration A2.
- Configuration C2 (Fig. 11c): No large vortices are present in the vertical plane, due to the presence of the two near-ground corner jets in the horizontal plane (see Fig. 9c and Fig. 10c). The collision of the two jets results in a strong upflow.
- Configuration D2 (Fig. 11d): A large vortex is present in the vertical plane, which, for this configuration, does reach the ground. Horizontal vortices underneath both the upstream and downstream roof result in an airflow down the stands and towards the field in the vertical mid-plane.

The configurations with a downward and upward sloped roof have similar general flow patterns in the vertical center plane, apart from the flow near the roof which is locally different.

5.1.3. Schematic representation

The 3D wind-flow patterns are more clearly and schematically displayed in Figure 12.

- Configuration A2 (Fig. 12a): The two large vortices between the upstream and downstream stand are driven by the side flow and by the interaction with the vertical vortex. The dotted arrows indicate the resulting flow direction underneath the roof of the stands.
- Configuration B2 (Fig. 12b): The flow is similar to that of configuration A2, because the side stands do not provide a large obstruction to the flow.
- Configuration C2 (Fig. 12b): The windshields provide a large obstruction to the flow and therefore a strong change in the flow pattern. The flow in the center part is directed upwards.
- Configuration D2 (Fig. 12d): Multiple vortices are present inside the stadium and interact with each other. The flow pattern is more complex than for the other three stand arrangements due to these vortices. Lower velocities occur inside the stadium.

These different wind-flow patterns will influence the raindrop trajectories and will lead to distinct wetting patterns on the stands.

5.2. Raindrop trajectories, stand wetting patterns and rain shelter percentages

Raindrop trajectories are calculated based on the steady wind-flow patterns described in the previous subsection, obtained with a reference wind speed U_{10} of 10 m/s. Raindrops with diameters of 0.5 mm, 1 mm, 2 mm and 5 mm are considered. The endpoints of around 10,000 raindrop trajectories for each raindrop diameter, which were obtained by releasing raindrops from a horizontal plane, mark the wetted area of the stands. The height at which the raindrops were released varies with raindrop diameter to ensure the impact of the raindrops inside the stadium. The results are presented as the ratio $A_{\text{wet}}/A_{\text{tot}}$, with A_{wet} the surface area that is wetted by WDR and A_{tot} the total surface area of the stands. This procedure was executed for the twelve stadium configurations, resulting in visualizations of raindrop trajectories, in visualizations of wetted surface areas on all stands and in overall percentages of wetted stand for each stadium configuration. The results are presented and discussed below.

5.2.1. Raindrop trajectories

Figure 13 shows raindrop trajectories obtained with the aforementioned procedure for a raindrop diameter of 1 mm (configurations A2-D2). The raindrops are released from a horizontal line in the vertical mid-plane. The figure clearly demonstrates the influence of the wind-flow pattern around the stadium on the raindrop trajectories.

- Configuration A2 (Fig. 13a): The raindrop trajectories inside the stadium are curved towards the upstream stand due to the reverse flow in the center plane, resulting in wetting of the upstream stand.
- Configuration B2 (Fig. 13b): Same observation as A2.
- Configuration C2 (Fig. 13c): The trajectories are more complex due to the larger complexity of the wind-flow pattern. Also in this case, the upstream stand is wetted.
- Configuration D2 (Fig. 13d): The smaller velocities inside the stadium lead to a smaller influence on the raindrop trajectories.

Figure 14 shows raindrop trajectories of 1 mm raindrops that are released from three horizontal lines at a height of 125 m, perpendicular to the flow direction. The three lines are located at a distance of 355 m, 300 m and 275 m in front of the upstream stand.

- Configuration A2 (Fig. 14a-c): The specific wind-flow pattern leads to wetting of the middle part of the upstream stand and the side parts of the downstream stand.
- Configuration B2 (Fig. 14d-f): Similar to A2, apart from the fact that also the lateral stands are wetted.
- Configuration C2 (Fig. 14g-i): The upstream stand is wetted, but the windshields seem effective in reducing wetting of the downstream and the lateral stands.
- Configuration D2 (Fig. 14j-l): The raindrop trajectories hardly reach any part of the stand.

5.2.2. Visualization of wetting patterns

Figures 15 and 16 show the surface areas of the stands that get wetted for each stadium configuration, for $U_{10} = 10$ m/s and for each raindrop diameter ($d = 0.5, 1, 2$ and 5 mm). These figures are in line with the previously discussed wind-flow patterns and raindrop trajectories.

- Stand arrangement A (Fig. 15): Due to the two large vortices between the upstream and downstream stand, part of the upstream stand gets wetted, especially for smaller raindrop diameters that are more sensitive to the wind-flow pattern and that can more easily be swept underneath the roof.
- Stand arrangement B (Fig. 15): Wetting of the upstream and downstream stand is quite similar to stand arrangement A. The lateral stands receive significant wetting.
- Stand arrangement C (Fig. 16): Wetting of the upstream and downstream stand is limited, except for roof type 3. The windshields are effective in shielding the lateral stands from WDR, especially for roof types 1 and 2. The windshields provide indirect shelter by changing the wind-flow pattern, as well as direct shelter by preventing the penetration of raindrops at the edges of the stands.
- Stand arrangement D (Fig. 16): Wetting is limited and only occurs at the bottom rows of the stands.

5.2.3. Percentages of wetted stand area

Figure 17 provides an overview of the percentages of wetted stand for the twelve configurations. The results of each stand arrangement are grouped into one bar chart. The following observations are made:

- Comparing the results for different stand arrangements with each other shows that the stand arrangement with the worst WDR shelter, irrespective of roof type, is stand arrangement B (Fig. 17b) (four stands, open corners, no windshields). As shown in Figure 15, this is for the largest part due to the absence of windshields for the side stands. The wetting percentages go up to 48% for the smallest raindrop diameter. The stand arrangement with the lowest overall percentages of wetted stand is the enclosed stadium (stand arrangement D) (Fig. 17d), with percentages that are below 10% for every roof type and raindrop diameter.
- Comparison of the results for different roof types with each other, for a given stand arrangement, shows that the use of a downward sloped roof results in the lowest percentage of wetted stand, followed by the flat roof. For all stand arrangements, the upward sloped roof shows the worst performance.

6. Discussion

In this section some limitations of this study will be addressed as well as recommendations for further studies.

The simulations in this study were performed steady-state and the results therefore represent mean values. They provide a general indication of the influence of stadium geometry on wind flow and WDR shelter. Further

research will include unsteady wind-flow effects on WDR. The simulations were conducted for only one reference wind speed ($U_{10} = 10$ m/s) and for only one wind direction, because varying all parameters in this study (stand arrangement, roof type, wind speed, wind direction, raindrop diameter, ...) would have resulted in an excessive amount of computations and results. The aim of this study was to perform a first analysis of the wind-flow patterns and raindrop trajectories for different stadium configurations. Further insight should be obtained by simulations with other wind speed values and wind directions. A complete set of simulations for different wind speed and wind directions would allow combining the CFD results with on-site wind and rain statistics to provide probability estimates of the wetting of the stands by WDR. Note that this study can also be extended with other roof types, e.g. curved roofs, roofs with larger overhangs, and other stand arrangements (three stands, two tiers instead of one tier, etc.).

To the knowledge of the authors, the first WDR study in stadia was published by Persoon et al. [6], who performed 2D CFD simulations to assess the WDR shelter for seven generic stadium configurations. The study showed that the roof design can strongly influence the size of the wetting areas on the stands. However, as mentioned in that study, 3D CFD simulations should be performed in order to capture the 3D flow pattern and to provide a better assessment of the influence of roof geometry on WDR shelter. The 3D CFD simulations of WDR as reported in this paper resulted in raindrop trajectories that differ from those found in the 2D simulations of Persoon et al. [6]. This difference is caused by the 3D wind-flow pattern which has different features compared to the 2D flow pattern. In the study of Persoon et al. [6], a large vortex in the vertical plane between the stands drove counter-rotating vortices underneath the roof. In the present study, this large vortex was only present for stand arrangement D. While there is a clear resemblance between the 2D and 3D wind-flow pattern for stand arrangement D, the flow underneath the roof is still quite different due to 3D flow effects (lateral flow underneath the roof). In spite of this, the main conclusions are the same. In both studies, wetting of the downstream stand is most pronounced for large raindrop diameters (2 mm and 5 mm), and the upstream stand remains nearly dry for each raindrop diameter. Furthermore, the upward sloped roof shows the worst WDR shelter, followed by the flat roof and the downward sloped roof.

7. Summary and conclusions

Although some studies on comfort in stadia were performed in the past, as well as studies using CFD simulation to assess the distribution of wind-driven rain (WDR) on building facades and over small-scale topography, to the knowledge of the authors, 3D CFD studies of WDR in stadia have not yet been performed. A full comfort study in stadia should also include rain shelter, as wetting by rain is a particularly drastic form of discomfort. The specific shapes of stadia, with an open roof and sometimes also open corners, give rise to particular wind-flow patterns and therefore also specific WDR distributions. There is almost no knowledge on these wind-flow patterns and WDR distributions. This information however is very important for stadium designers. The purpose of this paper was to provide detailed insight in and information on wind-flow patterns and WDR distributions in stadia. As stadia can have a wide range of geometries, twelve different generic stadia were considered and the influence of stadium geometry (roof type and stand arrangement) on the wind-flow patterns and WDR shelter has been studied.

The wind-flow pattern has been obtained using 3D steady RANS CFD simulations with the realizable k- ϵ turbulence model, after which raindrop trajectories have been determined using Lagrangian particle tracking. The use of CFD to calculate WDR in and around the stadia was supported by earlier CFD validation studies of WDR. The hybrid grid was based on a grid-sensitivity analysis with three different grids, showing the 1.5 million cell grid to be adequate for this study. CFD simulations were performed for a reference wind speed U_{10} of 10 m/s, one wind direction and one aerodynamic roughness length ($y_0 = 0.03$ m). A total of twelve stadium configurations has been evaluated based on wind-flow patterns, raindrop trajectories, wetting patterns and wetting percentages. The configurations were based on three roof types (downward, flat, upward) and four stand arrangements.

For the wind-flow patterns, the following conclusions are made:

- Two large horizontal counter-rotating vortices are present between the upstream and downstream stand for stand arrangements A (only two stands) and B (four stands, open corners, no windshields). These vortices are mainly driven by high velocities on the short edges of the stadium.
- No large vortices are present for stand arrangement C (four stands, open corners, windshields) due to the presence of the windshields that alter the flow pattern significantly. Instead, two jets are present on the field, originating from the upstream corners.
- Two horizontal counter-rotating vortices are present in stand arrangement D (enclosed stadium), however their size and velocity values are lower than for stand arrangements A and B.
- Only for stand arrangement D a large standing vortex is present between the upstream and downstream stand.

For WDR, the following conclusions are made:

- For the stadium configurations in this study, the type of stand arrangement is more important than the roof type.
- Wetting is most pronounced for stand arrangement B, due to the absence of windshields, and least pronounced for the enclosed arrangement D.
- For all stand arrangements in this study, a downward sloped roof provides the best WDR shelter, followed by the flat roof. The upward sloped roof provides the least WDR shelter.
- The presence of the two large vortices for stand arrangement A and B has a large effect on the wetting percentages of the upstream stand. The amount of wetted stand area is much larger for stand arrangement A and B compared to stand arrangement C and D.
- The windshields for stand arrangement C significantly improve the WDR shelter. Adding windshields prevents the formation of large vortices in the horizontal plane and provides direct shelter for the stands on the short edges of the stadium.

In terms of low wind velocities on the field and maximum WDR shelter, the enclosed stadium configurations with a downward sloped roof (D1) and a flat roof (D2) perform best of all configurations studied here, followed by the version with the upward sloped roof (D3).

The stadium configurations in this study were evaluated based on WDR shelter. However, which stadium configuration is the best in a given situation will be determined by a combination of design parameters. For example, better stadium ventilation by higher wind speeds on the field might be more important, to improve thermal comfort in warm/hot climates and to favor grass growth.

Acknowledgements

The simulations reported in this paper were supported by the Laboratory of the Unit Building Physics and Systems (BPS) of Eindhoven University of Technology.

References

- [1] Culley P, Pascoe J. Sports facilities and technologies. London: Routledge; 2009.
- [2] Szücs A, Perraudou P, Allard F. Assessment of visual comfort of spectators in stadia. Proceedings of the 21st international conference of passive and low energy architecture (PLEA), Geneva, Switzerland 2006;II: 609-12.
- [3] Szücs A, Moreau S, Allard F. Spectators' aerothermal comfort assessment method in stadia. *Build Environ* 2007;42(6): 2227-40.
- [4] Szücs A, Moreau S, Allard F. Aspects of stadium design for warm climates. *Build Environ* 2009;44(6): 1206-14.
- [5] Bouyer J, Vinet J, Delpéch P, Carre S. Thermal comfort assessment in semi-outdoor environments: Application to comfort study in stadia. *J Wind Eng Ind Aerod* 2007;95(9-11): 963-76.
- [6] Persoon J, van Hooff T, Blocken B, Carmeliet J, de Wit MH. On the impact of roof geometry on rain shelter in football stadia. *J Wind Eng Ind Aerod* 2008;96(8-9): 1274-93.
- [7] van Hooff T, Blocken B. Coupled urban wind flow and indoor natural ventilation modelling on a high-resolution grid: A case study for the Amsterdam ArenA stadium. *Environ Modell Softw* 2010;25(1): 51-65.
- [8] van Hooff T, Blocken B. On the effect of wind direction and urban surroundings on natural ventilation of a large semi-enclosed stadium. *Comput Fluids* 2010;39(7): 1146-1155.
- [9] Blocken B, Carmeliet J. A review of wind-driven rain research in building science. *J Wind Eng Ind Aerod* 2004;92(13): 1079-1130.
- [10] Choi ECC. Simulation of wind-driven rain around a building. *J Wind Eng Ind Aerod* 1993;46-7: 721-29.
- [11] Choi ECC. Parameters affecting the intensity of wind-driven rain on the front face of a building. *J Wind Eng Ind Aerod* 1994;53(1-2): 1-17.
- [12] Choi ECC. Determination of wind-driven rain intensity on building faces. *J Wind Eng Ind Aerod* 1994;51(1): 55-69.
- [13] Choi ECC. Numerical modelling of gust effect on wind-driven rain. *J Wind Eng Ind Aerod* 1997;72(1-3): 107-16.
- [14] Blocken B, Carmeliet J. Spatial and temporal distribution of driving rain on a low-rise building. *Wind Struct* 2002;5(5): 441-462.
- [15] Hangan H. Wind-driven rain studies. A C-FD-E approach. *J Wind Eng Ind Aerod* 1999;81: 323-31.
- [16] van Mook FJR. Driving rain on building envelopes. Ph.D. Thesis, Building Physics and Systems, Technische Universiteit Eindhoven, Eindhoven University Press, Eindhoven, The Netherlands, 2002, 198pp.

- [17] Blocken B, Carmeliet J. The influence of the wind-blocking effect by a building on its wind-driven rain exposure. *J Wind Eng Ind Aerod* 2006;94(2): 101-27.
- [18] Blocken B, Carmeliet J. Validation of CFD simulations of wind-driven rain on a low-rise building facade. *Build Environ* 2007;42(7): 2530-48.
- [19] Tang W, Davidson CI. Erosion of limestone building surfaces caused by wind-driven rain: 2. Numerical modeling. *Atmos Environ* 2004;38(33): 5601-09.
- [20] Abuku M, Blocken B, Nore K, Thue JV, Carmeliet J, Roels S. On the validity of numerical wind-driven rain simulation on a rectangular low-rise building under various oblique winds. *Build Environ* 2009;44(3): 621-32.
- [21] Briggen PM, Blocken B, Schellen HL. Wind-driven rain on the facade of a monumental tower: Numerical simulation, full-scale validation and sensitivity analysis. *Build Environ* 2009;44(8): 1675-90.
- [22] Arazi A, Sharon D, Khain A, Huss A, Mahrer Y. The windfield and rainfall distribution induced within a small valley: Field observations and 2-D numerical modelling. *Bound-Lay Meteorol* 1997;83(3): 349-74.
- [23] Choi ECC. Modelling of wind-driven rain and its soil detachment effect on hill slopes. *J Wind Eng Ind Aerod* 2002;90(9): 1081-97.
- [24] Blocken B, Carmeliet J, Poesen J. Numerical simulation of the wind-driven rainfall distribution over small-scale topography in space and time. *J Hydrol* 2005;315(1-4): 252-73.
- [25] Blocken B, Poesen J, Carmeliet J. Impact of wind on the spatial distribution of rain over micro-scale topography: numerical modelling and experimental verification. *Hydrol Process* 2006;20(2): 345-68.
- [26] Shih TH, Liou WW, Shabbir A, Yang ZG, Zhu J. A new kappa-epsilon eddy viscosity model for high Reynolds-number turbulent flows. *Comput Fluids* 1995;24(3): 227-38.
- [27] Franke J, Hellsten A, Schlünzen H, Carissimo B (Eds.). Best practice guideline for the CFD simulation of flows in the urban environment. COST Office Brussels; 2007.
- [28] Tominaga Y, Mochida A, Yoshie R, Kataoka H, Nozu T, Yoshikawa M, Shirasawa T. AIJ guidelines for practical applications of CFD to pedestrian wind environment around buildings. *J Wind Eng Ind Aerod* 2008;96(10-11): 1749-61.
- [29] Launder BE, Spalding DB, The numerical computation of turbulent flows. *Comput Method Appl M* 1974;3: 269-89.
- [30] Kim S-E, Choudhury D, A near-wall treatment using wall functions sensitized to pressure gradient, ASME FED Vol. 217, Separated and Complex Flows, 1995.
- [31] Best AC. The size distribution of raindrops. *Q J Roy Meteor Soc* 1950; 76(327): 16-36.
- [32] Gunn R, Kinzer GD. The terminal velocity of fall for water droplets in stagnant air. *J Meteorol* 1949;6:243-48.
- [33] Wieringa J. Updating the Davenport roughness classification. *J Wind Eng Ind Aerod* 1992;41(1): 357-68.
- [34] Fluent Inc. Fluent 6.3. User's Guide. Fluent Inc., Lebanon; 2006.
- [35] Kim SE, Choudhury D, Patel B. Computations of complex turbulent flows using the commercial code FLUENT", Proceedings of the ICASE/LaRC/AFOSRSymposium on Modelling Complex Turbulent Flows, Hampton, Virginia, 1997.
- [36] Franke J, Hirsch C, Jensen AG, Krüs HW, Schatzmann M, Westbury PS, Miles SD, Wisse JA, Wright NG. Recommendations on the use of CFD in wind engineering. In: van Beeck, J.P.A.J. (Ed.), COST Action C14, Impact of Wind and Storm on City Life Built Environment, Proceedings of the International Conference on Urban Wind Engineering and Building Aerodynamics. Von Karman Institute, Sint-Genesius-Rode, Belgium, 5-7 May 2004.
- [37] Cebeci T, Bradshaw P. Momentum transfer in boundary layers, Hemisphere Publishing Corporation; 1977.
- [38] Blocken B, Stathopoulos T, Carmeliet J. CFD simulation of the atmospheric boundary layer: wall function problems. *Atmos Environ* 2007;41(2): 238-52.

FIGURES

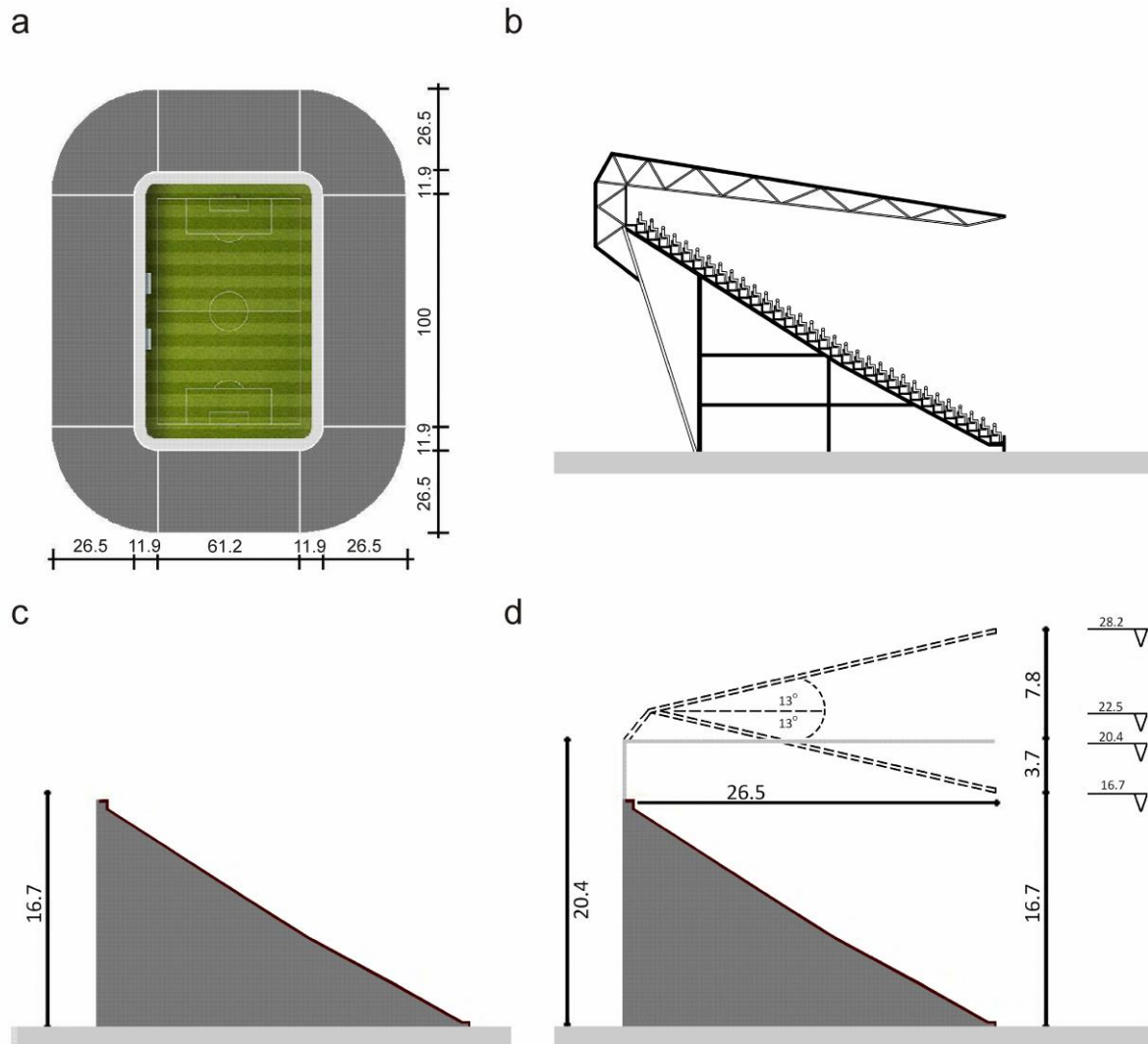


Fig. 1. (a) Top view of the stadium with dimensions in m, based on the stadium of AZ in Alkmaar, the Netherlands. (b) Vertical cross-section of the stand of the AZ stadium (© Zwarts and Jansma Architects, reproduced with permission). (c) Basic stand arrangement based on the AZ stadium. (d) Stand with the three roof types (upward sloping roof, flat roof, downward sloping roof) with dimensions in m.

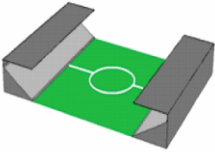
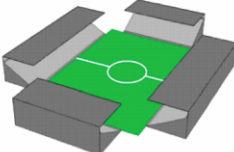
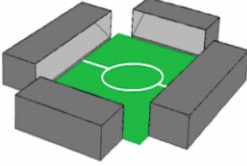
A. Only stands on long edges of stadium	B. Stands on all four edges of stadium; open corners	C. Four stands; open corners, windshields on edges of stands	D. Enclosed rectangular stadium
			
<p>1. </p> <p>2. </p> <p>3. </p>	<p>1. </p> <p>2. </p> <p>3. </p>	<p>1. </p> <p>2. </p> <p>3. </p>	<p>1. </p> <p>2. </p> <p>3. </p>

Fig. 2. Overview of the four stand arrangements and the three roof types, resulting in twelve different stadium configurations.

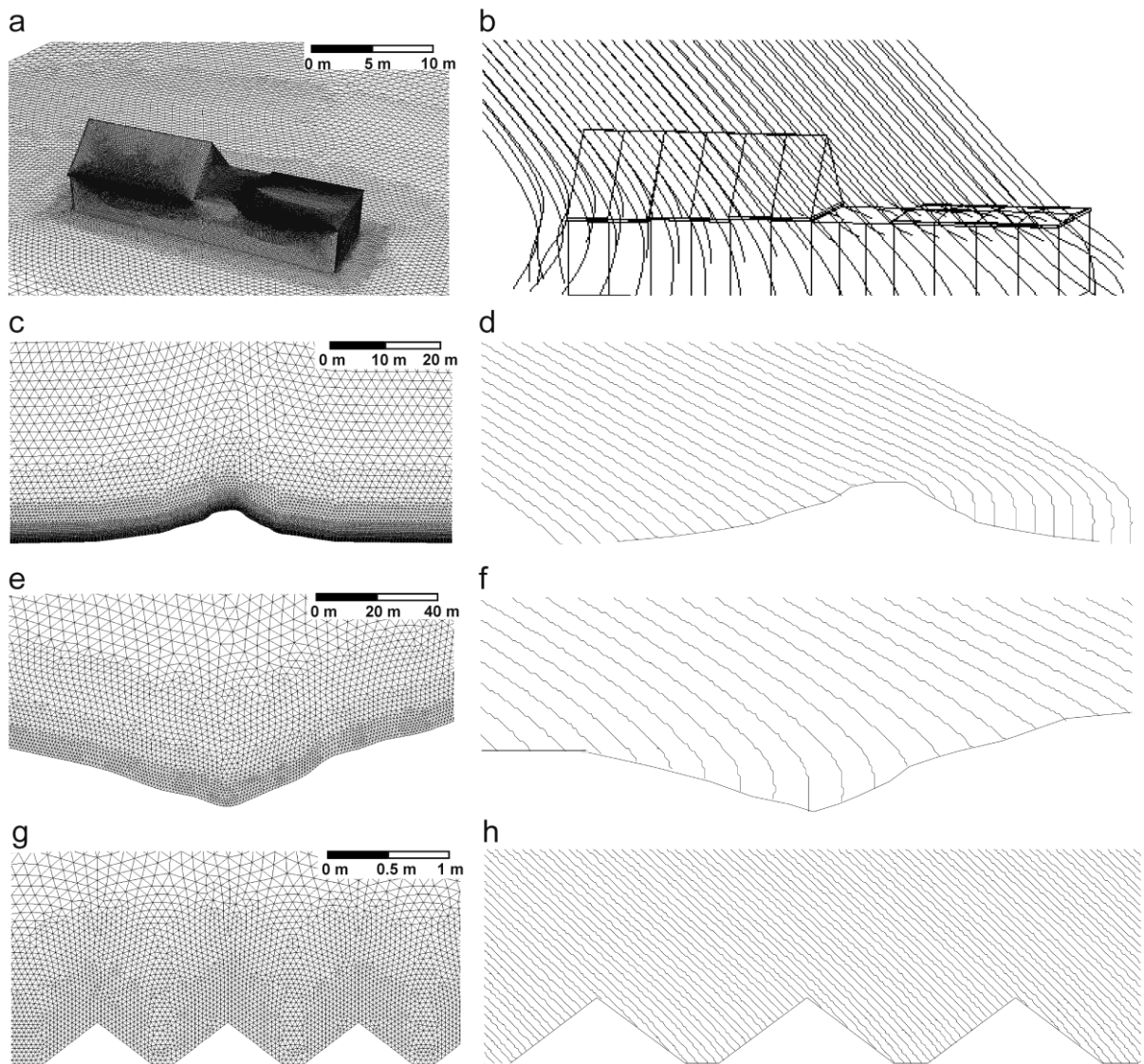


Fig. 3. Computational grids and raindrop trajectories used in previous CFD validation studies of WDR deposition on building facades and small-scale topographic features: (a-b) Grid and raindrop trajectories for the VLIET test building [17,18]. Raindrop trajectories are given for a reference wind speed U_{10} at 10 m height of 10 m/s and a raindrop diameter $d = 1$ mm; (c-d) Grid and raindrop trajectories (wind speed at 9 m height $U_9 = 4.6$ m/s; $d = 0.8$ mm) for an isolated hill [25]; (e-f) Grid and raindrop trajectories ($U_{10} = 5$ m/s; $d = 1$ mm) for a valley [25]; (g-h) Grid and raindrop trajectories ($U_1 = 4$ m/s; $d = 1$ mm) over a succession of ridges [25].

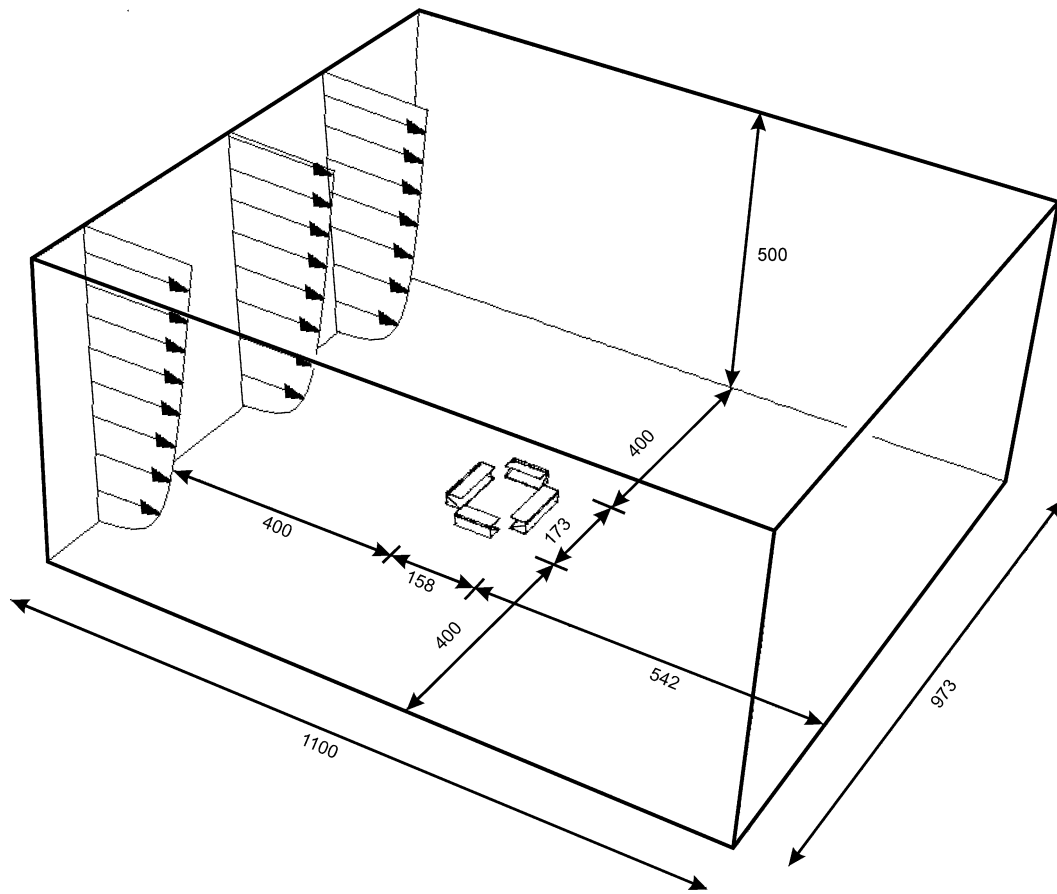


Fig. 4. View of the stadium in its computational domain. The large distances from the inlet and the top of the domain are required for the injection of the raindrops outside the wind-flow pattern that is influenced by the stadium.

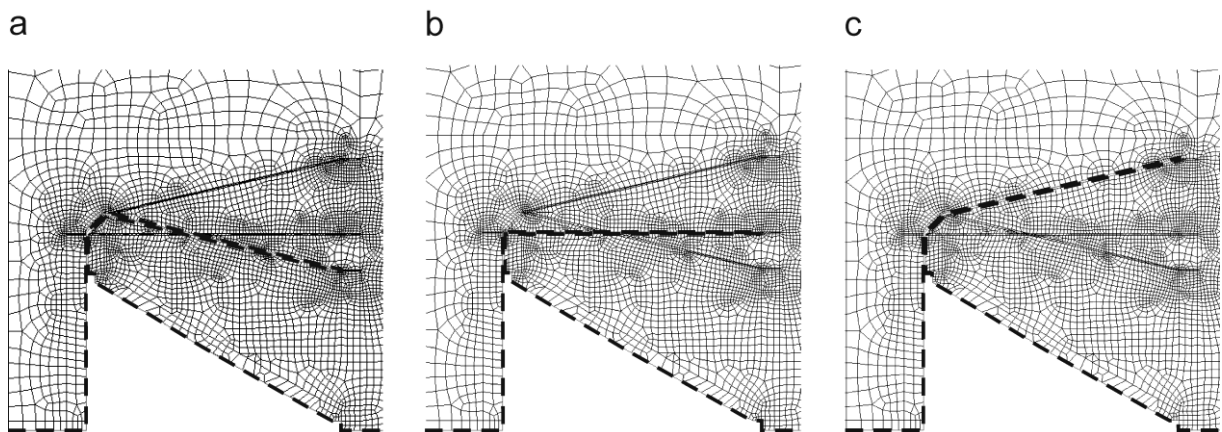


Fig. 5. Cross-sections of part of the computational grid, showing how the configurations with different roof geometry are extracted from the master grid. (a) Configuration with downward sloped roof; (b) configuration with flat roof; (c) configuration with upward sloped roof.

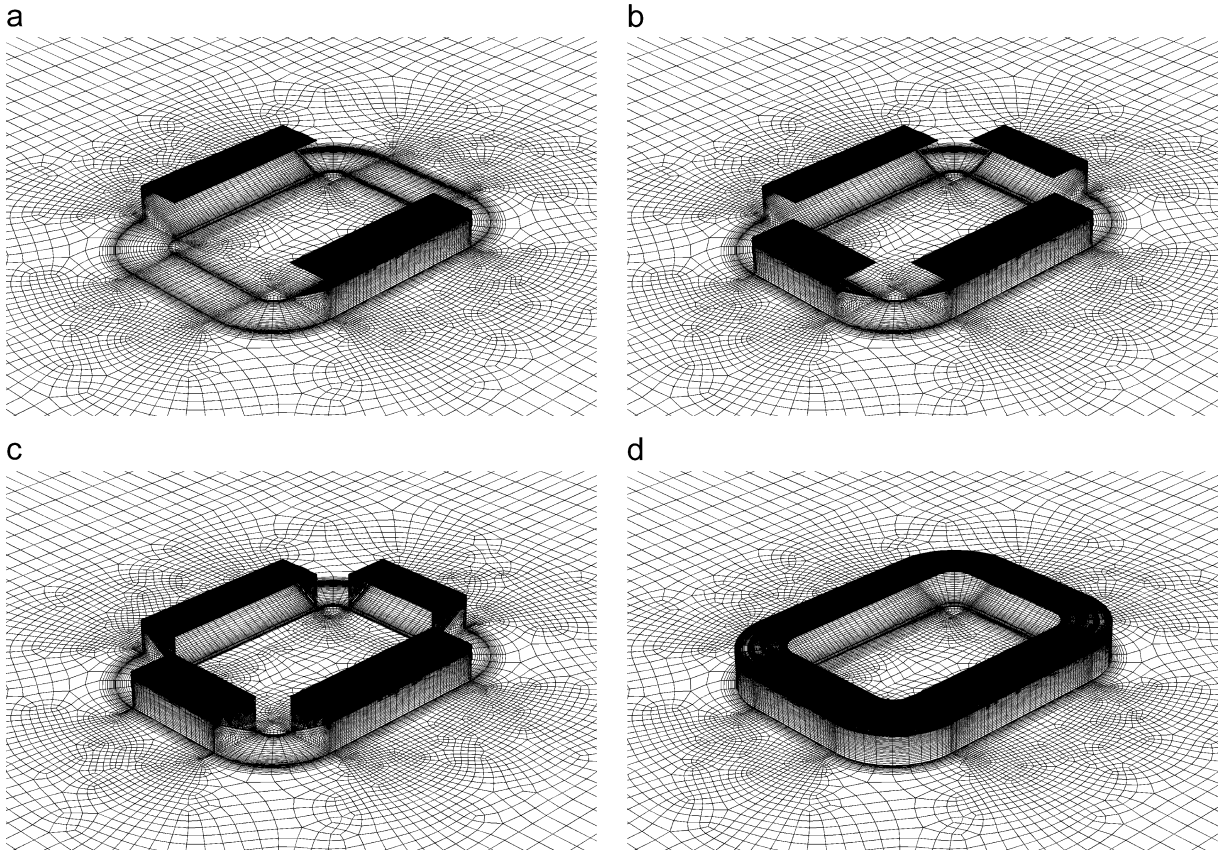


Fig. 6. Perspective view of the grid for the four stadium configurations with a flat roof. (a) A2; (b) B2; (c) C2; (d) D2.

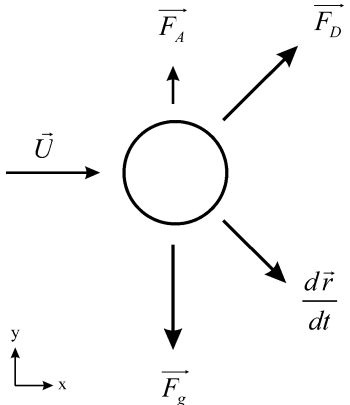


Fig. 7 Schematic representation of forces acting on a raindrop. Note that the drag force has a positive x component when the horizontal component of the wind velocity vector is larger than that of the raindrop velocity vector.

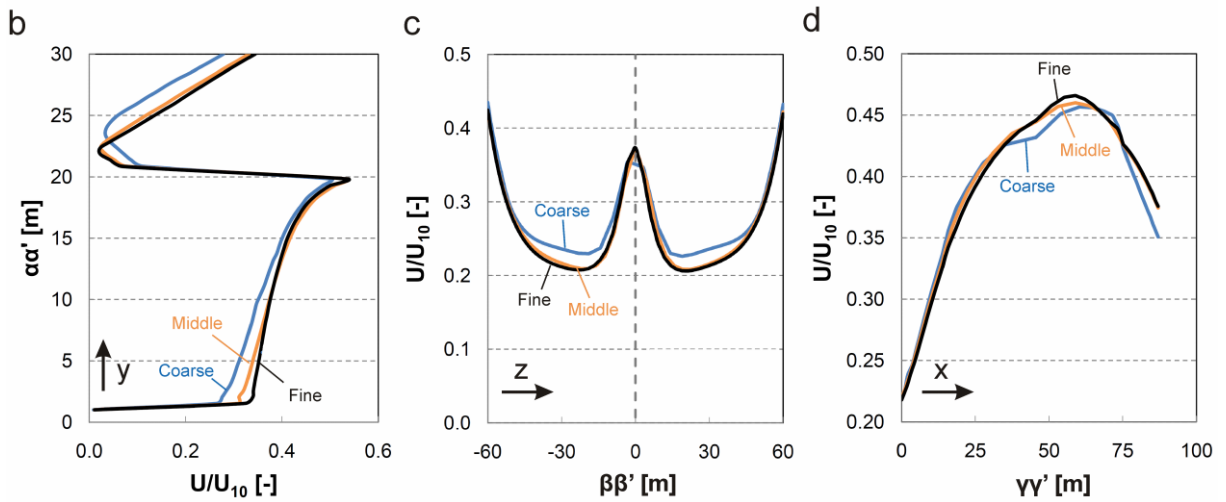
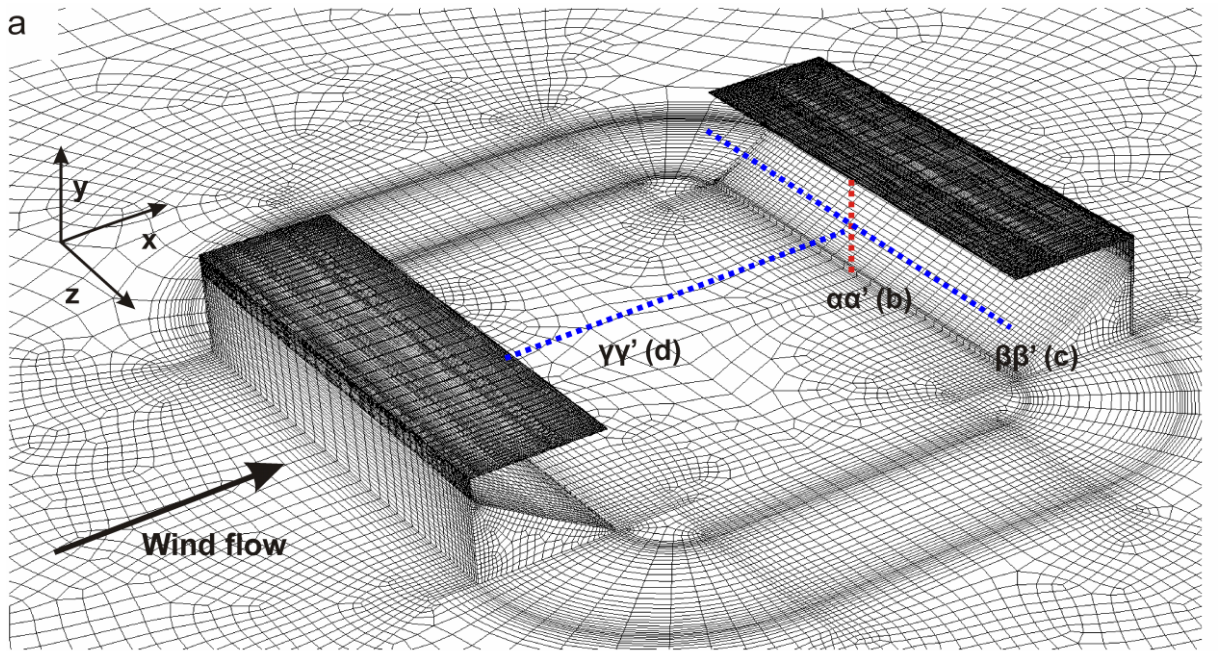


Fig. 8. (a) Stadium configuration used for the grid-sensitivity analysis. The dotted lines indicate the vertical and horizontal rakes along which the velocities are compared that are obtained with the three different grids. (b-d) Results showing U/U_{10} on: (b) vertical rake underneath the roof edge ($\alpha\alpha'$); (c) horizontal line underneath the roof ($y = 10$ m) perpendicular to the flow ($\beta\beta'$); (d) horizontal line ($y = 10$ m) in the streamwise direction in the center of the stadium ($\gamma\gamma'$).

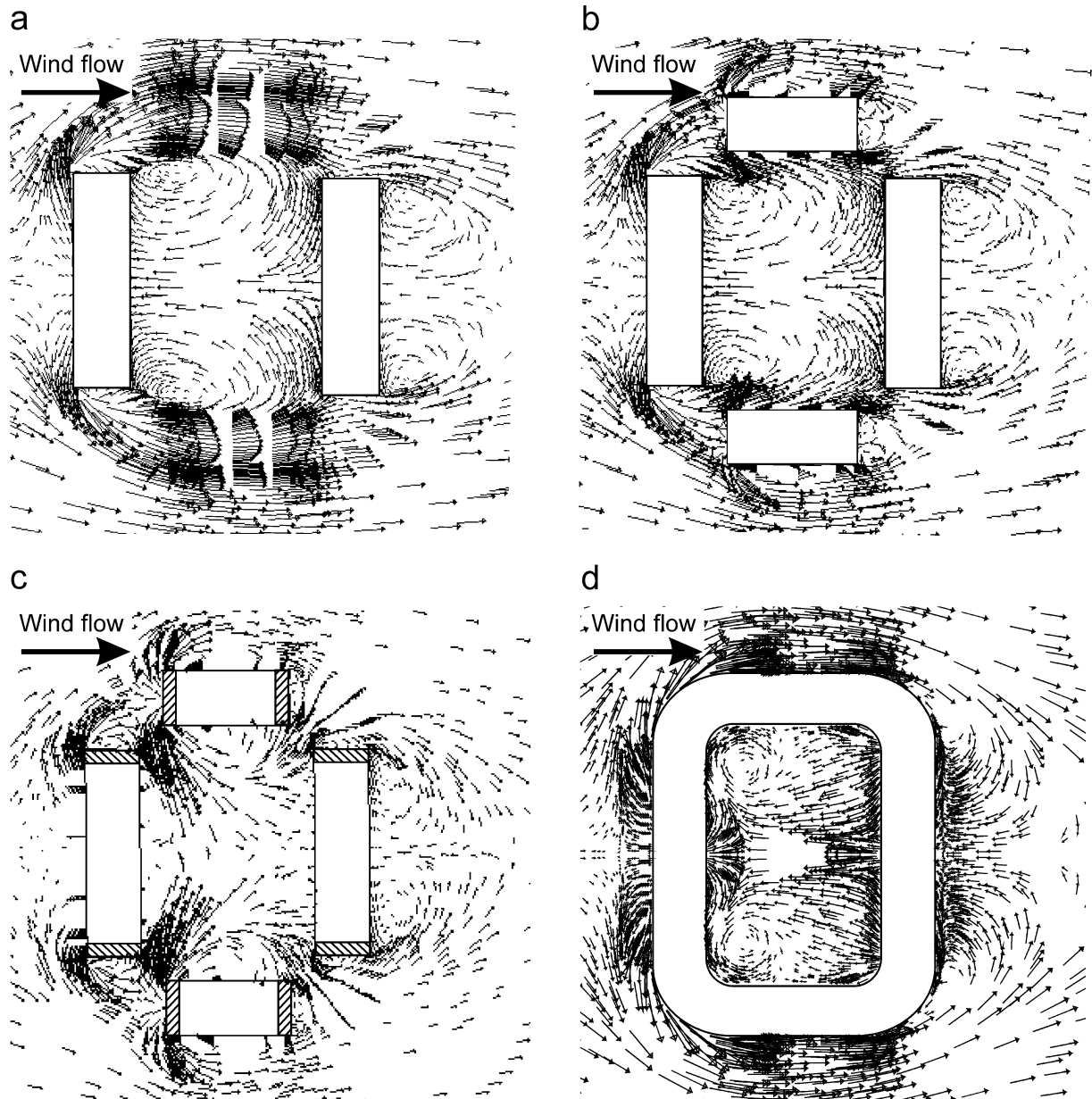


Fig. 9. Wind-flow patterns in and around the stadium, in a horizontal plane at a height of 1 m above the ground, for the four stadium configurations with a flat roof: (a) A2; (b) B2; (c) C2; (d) D2. In Fig. c, the windshields are schematically indicated by the hatched areas.

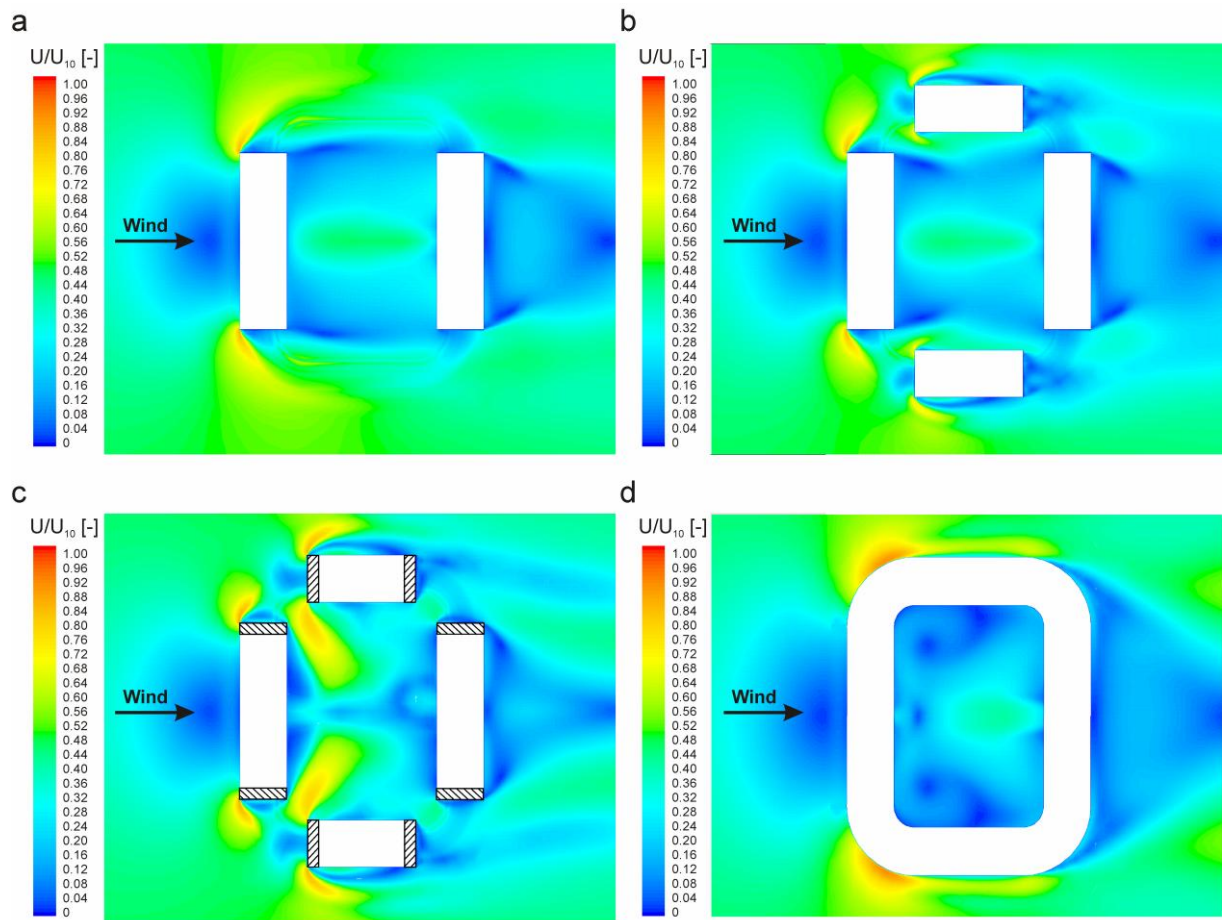


Fig. 10. Contours of dimensionless velocity magnitude (U/U_{10}), in a horizontal plane at a height of 1 m above the ground, for the four stadium configurations with a flat roof: (a) A2; (b) B2; (c) C2; (d) D2.

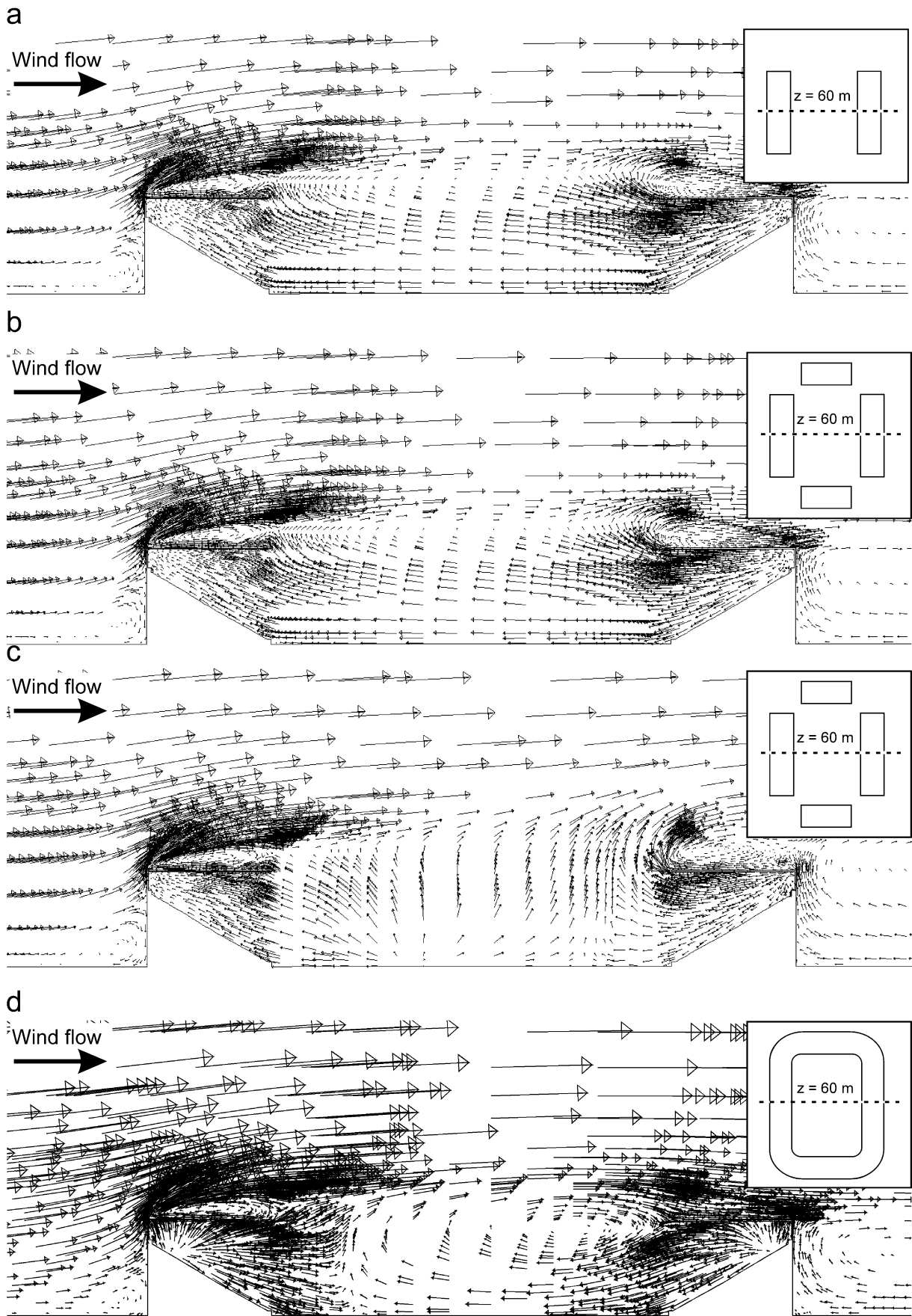


Fig. 11. Wind-flow pattern in a vertical cross-section in the middle of the stadium ($z = 60$ m), for the four stadium configurations with a flat roof: (a) A2; (b) B2; (c) C2; (d) D2.

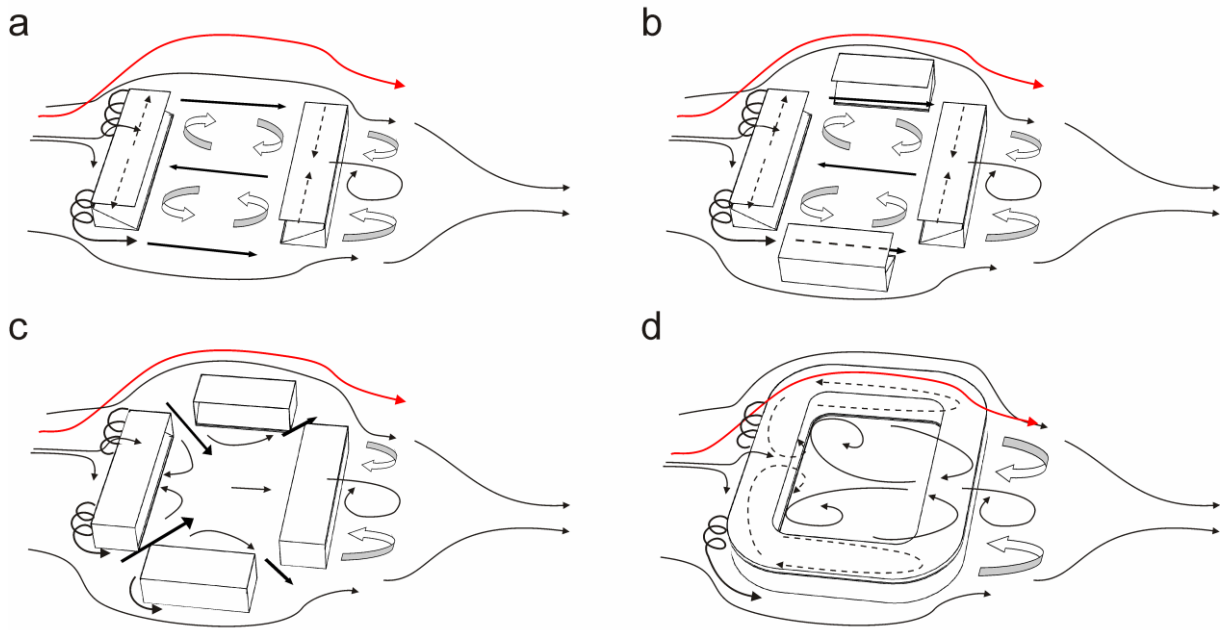


Fig. 12. Schematic representation of the wind-flow pattern in and around the stadium for four stadium configurations: (a) A2; (b) B2; (c) C2; (d) D2.

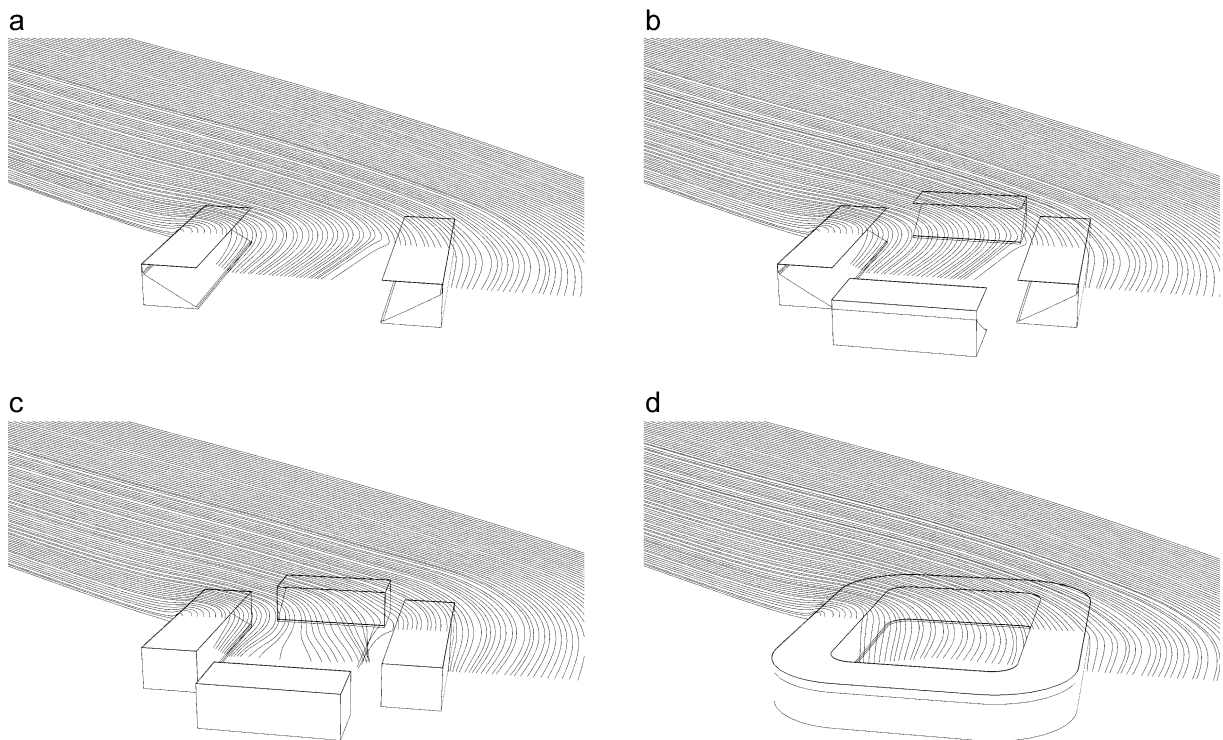


Fig. 13. Raindrop trajectories for 1 mm raindrops, released from a horizontal line parallel to the flow direction, for $U_{10} = 10$ m/s and four stadium configurations: (a) A2; (b) B2; (c) C2; (d) D2.

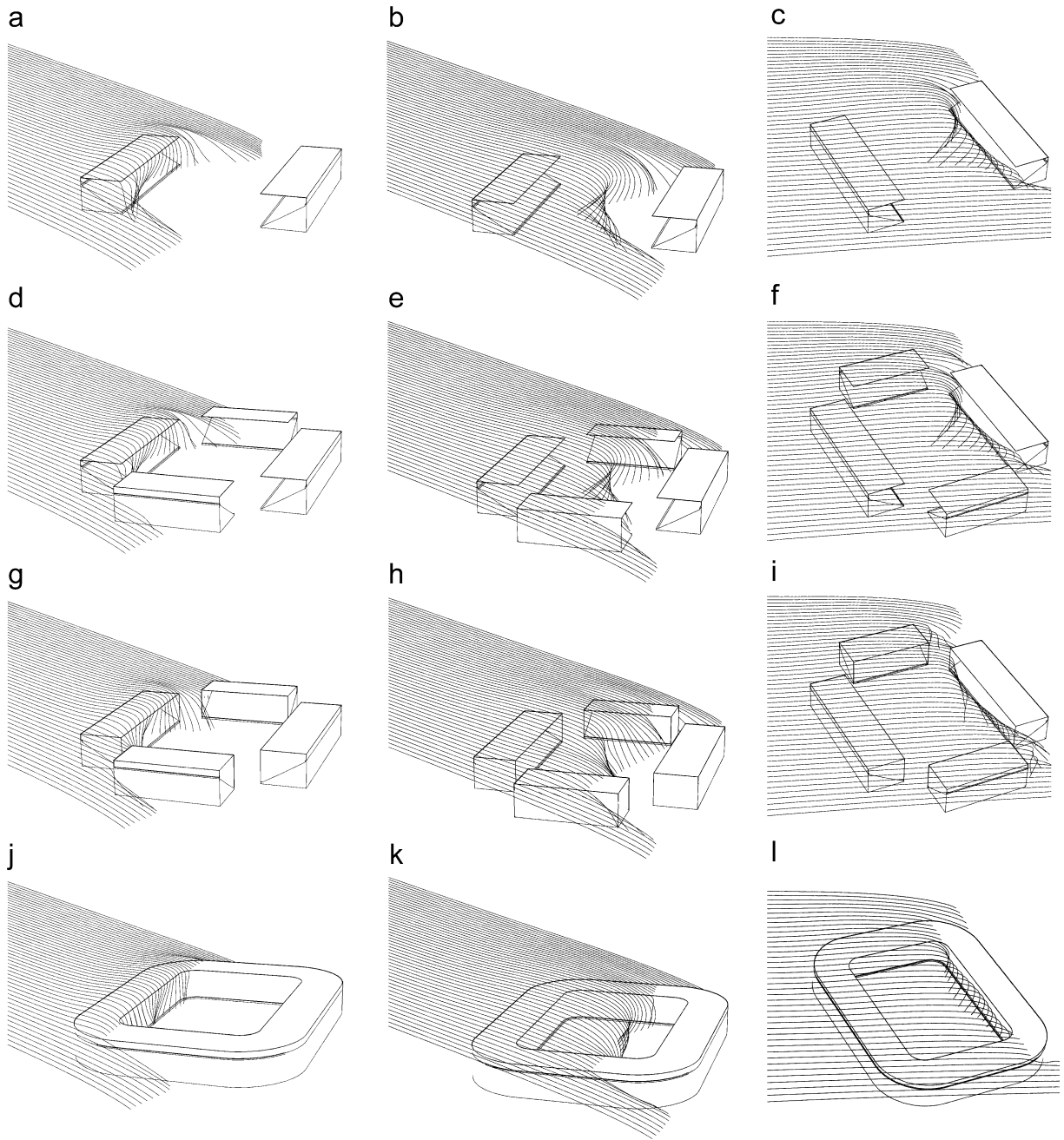


Fig. 14. Raindrop trajectories for 1 mm raindrops, released from three horizontal lines at a height of 125 m, perpendicular to the flow direction, for $U_{10} = 10$ m/s and for four stadium configurations: (a-c) A2; (d-f) B2; (g-i) C2; (j-l) D2.

Stand arrangement	Roof type	Drop diameter: 0.5 mm	Drop diameter: 1 mm	Drop diameter: 2 mm	Drop diameter: 5 mm
A	1.				
A	2.				
A	3.				
B	1.				
B	2.				
B	3.				

Fig. 15. Overview of wetted stand areas for stand arrangements A and B combined with the three different roof types, for $U_{10} = 10$ m/s and for raindrop diameters $d = 0.5, 1, 2$ and 5 mm.

Stand arrangement	Roof type	Drop diameter: 0.5 mm	Drop diameter: 1 mm	Drop diameter: 2 mm	Drop diameter: 5 mm
C	1.				
C	2.				
C	3.				
D	1.				
D	2.				
D	3.				

Fig. 16. Overview of wetted stand areas for stand arrangements C and D, combined with the three different roof types, for $U_{10} = 10$ m/s and for raindrop diameters $d = 0.5, 1, 2$ and 5 mm.

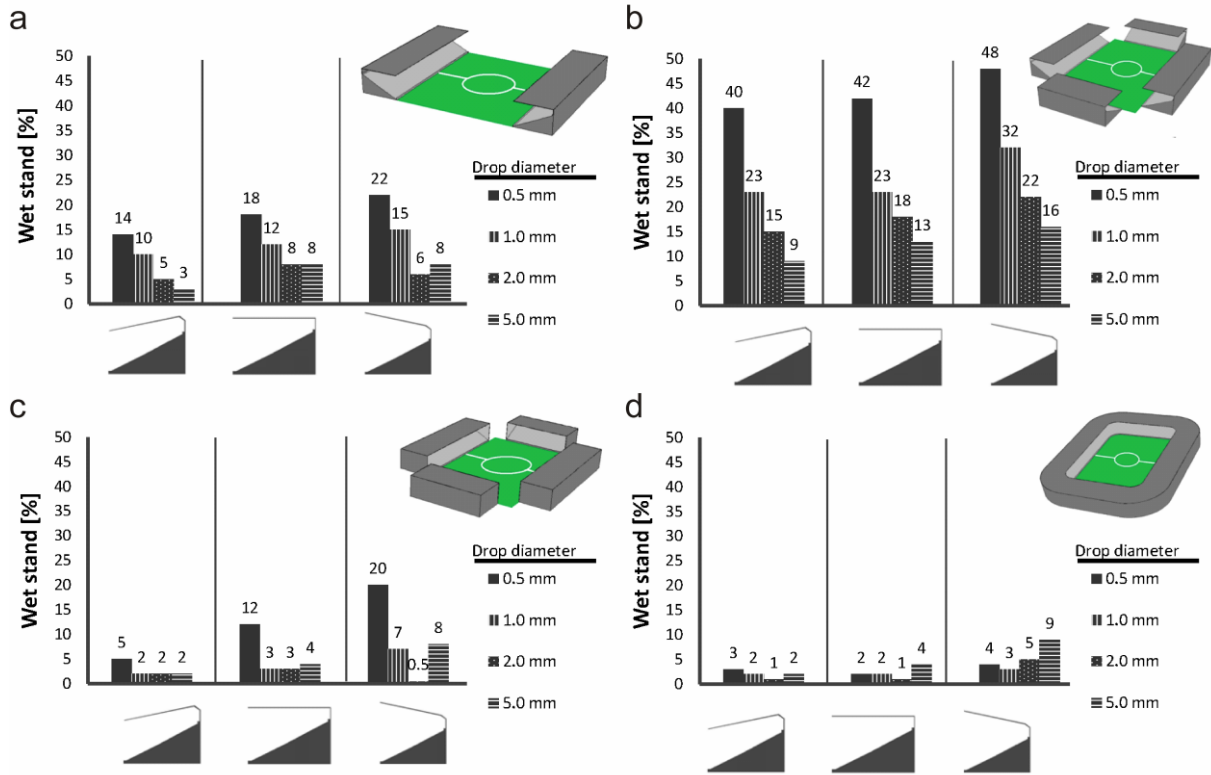


Fig. 17. Percentages of wetted stand for the twelve stadium configurations, for $U_{10} = 10$ m/s and for raindrop diameters $d = 0.5, 1, 2$ and 5 mm. (a) A1-A3; (b) B1-B3; (c) C1-C3; (d) D1-D3.